Journal of Energy Storage 154 (2026) 121028

Contents lists available at ScienceDirect

Journal of Energy Storage

journal homepage: www.elsevier.com/locate/est

Research papers

Deep learning for decoding lithium plating in lithium-ion batteries from post-mortem images

Thorsten Tegetmeyer-Kleine [a,b,c,*], Heinrich Ditler [a,b,c], Gereon Stahl [a,b,c], Christiane Rahe [a,b,c], Dirk Uwe Sauer [a,b,c,d], Weihan Li [a,b,c,**]

[a] Center for Aging, Reliability and Lifetime Prediction of Electrochemical and Power Electronic Systems (CARL), RWTH Aachen University, Campus-Boulevard 89, Aachen, 52074, Germany
[b] Institute for Power Electronics and Electrical Drives (ISEA), RWTH Aachen University, Campus-Boulevard 89, Aachen, 52074, Germany
[c] Juelich Aachen Research Alliance, JARA-Energy, Templergraben 55, Aachen, 52056, Germany
[d] Helmholtz Institute Muenster (HI MS), IMD-4, Forschungszentrum, Juelich, Germany

ARTICLE INFO

Keywords:
Lithium plating
Deep learning
Variational autoencoder
Battery diagnostics
Computer vision

ABSTRACT

Lithium plating is a safety-critical parasitic process in lithium-ion batteries that reduces efficiency and usable capacity and elevates safety risk. Conventional assessment relies on manual post-mortem inspection, but manual inspection is slow, subjective, and hard to scale. This work introduces an automated computer-vision methodology for the systematic characterization of lithium plating. A convolutional attention-based variational autoencoder with k-means clustering identifies and quantifies plating features from high-resolution flatbed scans. The model was trained on the complete imaging set (over 5000 scans from more than 60 cells) to construct a descriptive morphological atlas of the experimental matrix. A fixed condition-complete subset of 13 cells ($N = 1,092$ scans) was used solely as a convergence monitor and for the quantitative trend analyses reported in this work. The learned two-dimensional latent space disentangles C-rate (1C to 4C) and temperature (−20°C to −5°C) while tracking plating severity and spatial uniformity; its coordinates correlate monotonically with the stripping capacity Q_{strip}, providing a quantitative bridge between surface morphology and electrochemical indicators. Spearman analysis confirms these latent axes encode operating conditions: Dim1 vs Temp $|\rho|$=0.93, Dim2 vs Temp $|\rho|$=0.84, Dim1 vs C-rate $|\rho|$=0.75, Dim2 vs C-rate $|\rho|$=0.72. The approach delivers objective and scalable diagnostics that complement non-invasive electrical methods and demonstrates that computer vision can capture operating-condition effects directly from post-mortem images, enabling risk maps and high-throughput screening to support safer and longer-lasting lithium-ion battery systems.

1. Introduction

Achieving fast yet safe charging of lithium-ion batteries under realistic operating conditions remains the key technical barrier to widespread electrification. Real-world temperature, state-of-charge, aging, and cell-to-cell variability strongly modulate intercalation kinetics and plating risk, so protocols that are safe in the lab can fail or be overly conservative in the field. Fast charging at low temperature can trigger lithium plating when Li^+ does not intercalate into graphite quickly enough and metallic lithium deposits on the anode surface [1,2]. Lithium plating consumes cyclable lithium, reduces capacity and potentially forms dendrites that pierce the separator, creating internal shorts and, in severe cases, leading to thermal runaway [3–5].

In practice, detecting and managing lithium plating relies on complementary diagnostics operating at different scales, motivating spatially resolved, quantitative analysis. These methods can be categorized into two classes: non-invasive and invasive. Non-invasive diagnostics such as differential voltage analysis (DVA) [6], Electrochemical Impedance Spectroscopy (EIS) [7,8], and Distribution of Relaxation Times (DRT) [9] provide indirect indicators of lithium plating. In DVA, an early $\mathrm{d}V/\mathrm{d}Q$ "stripping" feature at the start of discharge serves as an indicator for reversibly plated lithium, often quantified by the extra capacity Q_{strip} [6,10]. In EIS, the immediate post-charge emergence and subsequent relaxation of a low-frequency process (frequently observed as a transient inductive loop) signals plating/stripping kinetics [7,8]. In DRT, plating manifests as a new or shifted time constant associated

* Corresponding author.
** Corresponding author.
E-mail addresses: ttegetmeyer-kleine@isea.rwth-aachen.de (T. Tegetmeyer-Kleine), weihan.li@isea.rwth-aachen.de (W. Li).

https://doi.org/10.1016/j.est.2026.121028
Received 22 October 2025; Received in revised form 20 January 2026; Accepted 7 February 2026
Available online 20 February 2026

with anode charge-transfer processes [9]. These signatures are valuable for protocol screening, yet they average responses over the entire cell and therefore cannot localize where plating initiates [9]. To address the lack of spatial resolution in global electrical measurements, recent advances in internal sensing and distributed diagnostics have emerged. Implanted potential sensing separators and stable reference electrodes now allow for the direct, in situ monitoring of local anode potentials and plating conditions [11,12]. Concurrently, novel distributed characterization methods, such as operando magnetic field mapping and kinetic evolution studies, provide a more comprehensive view of spatially inhomogeneous reactions and the dynamic onset of lithium plating [13,14].

To bridge cell-averaged signals with structural evidence, correlative studies have combined electrical stripping with imaging to validate the onset of plating and to anchor interpretation of electrical features [3, 15]. Building on this, operando probes introduce spatial and temporal context on intact cells. Neutron diffraction (ND) tracks the graphite peak to quantify local lithiation and attributes surplus signal beyond full lithiation to metallic lithium [16], while ^{7}Li nuclear magnetic resonance (NMR) detects metallic lithium directly via its Knight-shifted resonance near 260 ppm, separated from the ionic signal near 0 ppm [17]. Beyond neutron and NMR, ultrasound-based scanning acoustic imaging offers a complementary, non-destructive operando modality. Open-hardware scanning acoustic microscopy (SAM) resolves aging patterns, in-situ SAM enables layer-resolved tomography, and recent operando work visualizes lithium plating in multilayer pouch cells [18–20]. While SAM provides valuable operando insight (e.g., 75 μm pixel size in multilayer pouch cells [20]), this post-mortem optical pipeline achieves substantially finer spatial resolution across entire electrodes, which is crucial for localized quantification. Although powerful, these operando techniques require specialized instrumentation and are not easily deployed for high-throughput studies. When broad coverage and high spatial details are needed, post-mortem analysis remains the most direct way by using optical microscopy, scanning electron microscopy (SEM), and glow-discharge optical-emission spectroscopy (GD-OES) depth profiling to map morphology and distribution. In commercial formats, temperature and mechanical pressure gradients drive highly inhomogeneous lithium plating [21–23]. Optical and electrochemical studies under realistic fast charge protocols have visualized lithium plating fronts and have informed mitigation strategies, while loading and high current further shape failure modes [24–29]. However, the volume and complexity of these measurements, together with the need for structural context, make manual interpretation a bottleneck. Manual interpretation of large image sets remains slow, subjective, and difficult to scale, underscoring the need for objective post-mortem workflows that convert images into quantitative, localized maps and interface cleanly with cell-level electrical signatures. These constraints motivate automated image analysis. Image-based analysis has become central to high/throughput materials and biomedical diagnostics [30,31]. Convolutional neural networks (CNNs) and variational autoencoders (VAEs) learn compact latent representations that capture subtle texture and morphology, and simple clustering methods such as k-means can separate latent features into coherent groups [32,33]. Recent work has demonstrated that these tools transfer effectively to electrochemical imaging, reducing manual effort while enabling objectivity [34–36].

Despite this method, key gaps remain. Routine post-mortem workflows still depend on manual visual inspection, which is time-consuming, expensive, subjective, and difficult to scale. The field lacks an objective and scalable method that localizes lithium plating, quantifies its spatial patterns, and links those patterns to operating conditions while interfacing cleanly with cell level electrical signatures. Computer vision for post-mortem lithium plating analysis is only emerging, with few open datasets. Current methods flag plating yet need rapid, spatially resolved quantification at scale. Closing this gap is critical as fast charging becomes routine [37]. Fast charging is moving from laboratory validation to widespread deployment in transportation and grid services [37,38]. Manufacturers and researchers require rapid and reproducible methods to screen protocols, assess failure risk, and provide feedback on design changes for thermal management and mechanical compression [39]. An automated and quantitative mapping of lithium plating shortens the iteration cycle, reduces expert time, supports quality assurance, and creates a bridge between cell-level electrical signals and spatially resolved ground truth [40,41].

To meet these needs, this work presents an automated, unsupervised, label-free quantification and categorization computer vision pipeline for post-mortem characterization of lithium plating across entire electrodes at scale, aligned with C-rate and temperature. A convolutional attention-based variational autoencoder (ConvAttnVAE) with k-means clustering learns from high-resolution flatbed scans to identify, cluster, and quantify lithium plating features without labeled data. Validated on scans from more than 60 cells cycled across temperatures and charge rates with 84 sheets per cell, the model visualizes expected trends with stronger lithium plating at lower temperatures and higher charge rates and reveals a two-dimensional latent space that disentangles operating conditions (C-rate and temperature) while tracking plating severity and heterogeneity. The learned latent coordinates correlate with stripping capacity Q_{strip}, turning image texture into quantitative indicators for diagnostics. By converting large-scale post-mortem imagery into objective features, the pipeline enables fast-charge risk mapping and high-throughput protocol screening, delivering scalable diagnostics that complement non-invasive electrical methods and support the development of safer and longer-lasting lithium-ion battery systems.

Beyond automating post-mortem inspection, the central contribution is a continuous plating-severity coordinate learned in an unsupervised manner from full-electrode scans. This 2D representation aligns with the two controlled drivers (C-rate, temperature) and converts morphology into quantitative indicators that track Q_{strip}, enabling risk maps and protocol triage without labels.

2. Methodology

The overall workflow (see Fig. 1) consists of three stages: **(i) Data acquisition and preprocessing:** Cells are cycled over a matrix of temperatures and charge rates. After cycling, cells are opened and the harvested electrode sheets are imaged on a flatbed scanner to obtain high-resolution images. Sheet regions are extracted, followed by basic normalization and quality control. In many cases, lithium plating is already observable by eye as distinct textural patterns. **(ii) Representation learning:** Image tiles are encoded with a VAE, yielding a compact latent vector for each tile that captures morphology and texture relevant to plating. **(iii) Clustering and analysis:** The latent embeddings are clustered to group tiles with similar appearance, and cluster distributions are correlated with operating conditions. Clusters enriched at low temperature and high charge rate correspond to visually plated surfaces, enabling data-driven identification and characterization of plated sheets.

2.1. Experimental setup and data generation

The cells under investigation originate from a Tattu TAA-850-3S-75-XT3 battery pack. Each pouch cell is rated at 850 mAh with a datasheet voltage window of 3.0–4.2 V. The chemistry is lithium cobalt oxide (LCO) vs. graphite with an EC:PC:DMC electrolyte containing $LiPF_6$ conductive salt (identified via EDX/ICP-OES and GC–MS). Across the batch, the initial capacity ranged from 846 to 893 mAh (mean 873 mAh), and the 1 kHz AC resistance was 3.14–3.63 mΩ (mean 3.36 mΩ). A typical cell weighed 20.81 g and measured approximately 2.9 cm × 5.0 cm × 0.7 cm. The jelly-roll comprised 42 anode sheets (single-side coating thickness 26–29 μm on a 6 μm Cu current collector) and 41 cathode sheets (single-side coating thickness 23 μm on a 14 μm Al current collector), separated by a 15 μm separator. Individual cells

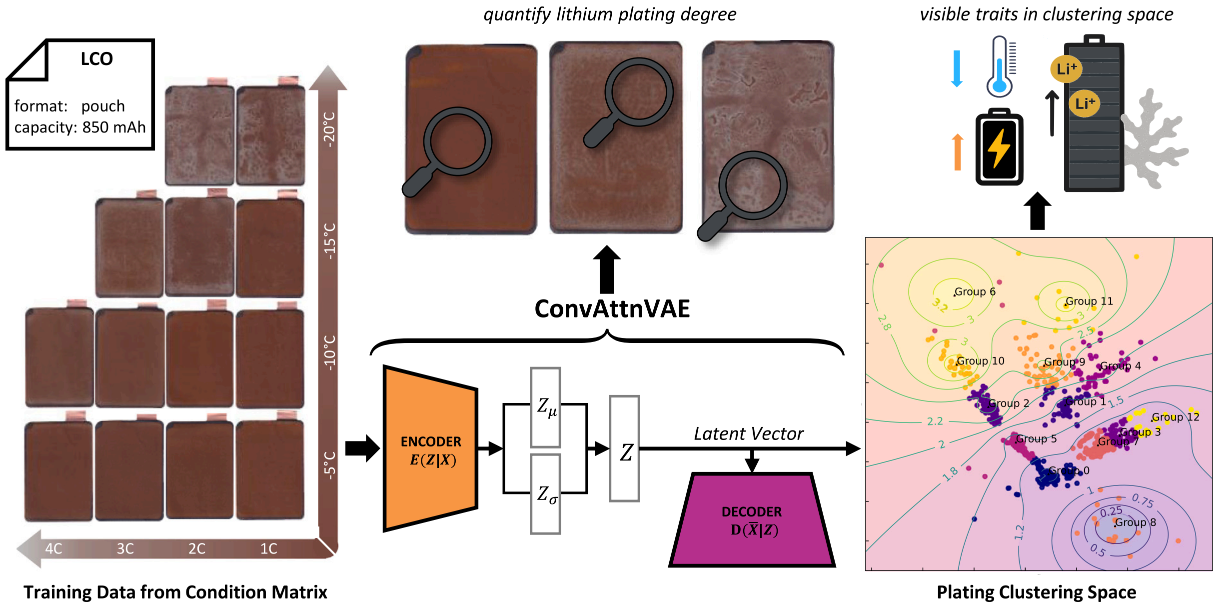

Fig. 1. Unsupervised workflow for lithium plating analysis: label-free plating analysis from post-mortem scans. LCO pouch cells (850 mAh) are cycled across a temperature–C-rate condition matrix. Post-mortem electrode surface scans are preprocessed and embedded using a convolutional attention VAE (ConvAttnVAE). The encoder maps each image to a latent vector Z (parameterized by Z_μ and Z_σ), and clustering in this latent space yields a data-driven "plating space" that organizes electrodes by morphology and severity for subsequent analysis.

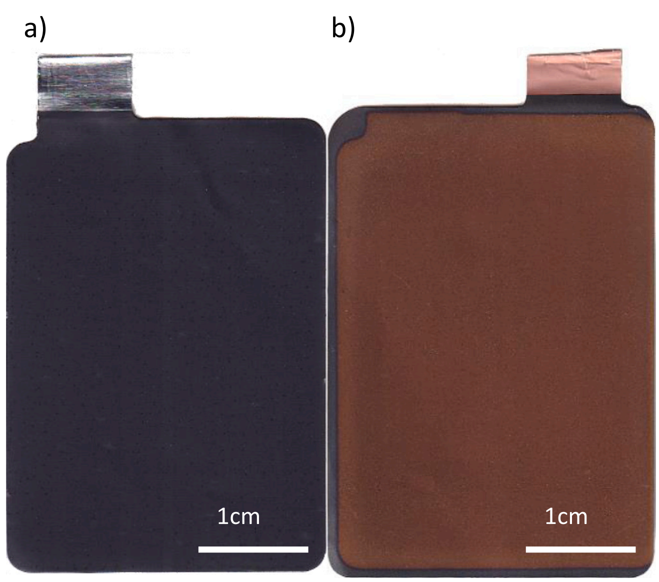

Fig. 2. Electrode surfaces. (a) Extracted cathode showing the textured LCO active material. (b) Anode at 100% state of charge, where the reddish-brown color reflects lithium intercalation into graphite [15]. (For interpretation of the references to color in this figure legend, the reader is referred to the web version of this article.)

were separated and mounted in a custom mechanical fixture consisting of two aluminum plates, guide rails, and bolt-guided springs, providing uniform clamping pressure while acting as a passive heat sink. This arrangement ensured reproducible mechanical conditions and passive cooling, which are necessary to control thermal gradients and prevent artifacts during cycling. All tests were conducted in a climate chamber (Binder MK 53) to maintain a stable temperature environment [15].

To visualize the internal state, the cell was opened post-cycling under an inert argon atmosphere (O_2 <1 ppm, H_2O<0.3 ppm) to avoid corrosion. Fig. 2 shows typical cathode and anode surfaces. The cathode displays the textured lithium cobalt oxide (LCO) coating, while the anode exhibits a reddish-brown color consistent with full lithiation [15]. These visual inspections guided the subsequent image-based analyses.

2.2. Cycling protocol, post-mortem imaging and data preprocessing

Each cell was cycled following the protocol detailed by Ditler et al. [15]. After conditioning cycles at C/10, constant-capacity charges at different C-rates were applied to achieve defined states of charge. Cells then underwent either a stripping test (C/20 discharge) or a 5 h open-circuit rest. A C/10 cycle between each high-rate charge step helped restore baseline conditions. Separate cells were used for each temperature (−5°C to −20°C) to prevent cumulative degradation effects.

Immediately after the final charge/discharge step, cells were opened in the glove box, and electrodes were flattened and scanned using a Canon CanoScan LiDE 300 at 600 DPI (42 μm pixel width). Uniform illumination and fixed geometry ensured comparable imaging conditions across all samples. More than 60 cells were imaged, yielding over 5 000 anode scans. To maximize interpretability, Ditler et al. [15] applied an automated ROI-detection and cleaning pipeline: grayscale conversion and median blurring, binary thresholding with morphological opening, and contour-based square detection and ordering to isolate the 42 sheets per scan. Their work also confirmed that bright spots correspond to metallic lithium rather than salt deposits, establishing confidence in the label-free identification of lithium plating.

An illustrative subset of the dataset is displayed in Fig. 3. Each row corresponds to a different temperature (from −5°C to −20°C), and columns vary the charging C-rate (from 1 C to 4 C). The absence of images at certain low temperatures/high C-rates results from cells reaching voltage limits, preventing further cycling. Consistency in image input is essential for machine learning. The raw scans were slightly variable in size. Thus, all images were resized directly to 960 × 640 pixels without cropping or padding. This simple resizing preserved full field-of-view while standardizing the input tensor shape. The original three-channel (RGB) format was maintained, as color cues were considered informative for detecting plating features.

To construct a comprehensive morphological atlas of the experimental set, the ConvAttnVAE was trained in a one-stage, descriptive setting.

Fig. 3. Experimental condition matrix (temperature–C-rate) with representative anode scans. Representative post-mortem anode surface scans are arranged by charging C-rate (1–4 C) and temperature (−5°C to −20°C), defining the experimental design used throughout the manuscript. At the most extreme low-temperature/high-C-rate combinations, charging terminated early due to voltage limits, so no sample is available. (For interpretation of the references to color in this figure legend, the reader is referred to the web version of this article.)

The objective of this work is dimensionality reduction and unsupervised clustering of the degradation patterns present in the acquired post-mortem image set, rather than supervised prediction on an unseen test population. Consequently, no permanently held-out test set was defined for predictive benchmarking. For quantitative, condition-wise analyses that require a complete temperature–C-rate grid, a fixed condition-complete base set consisting of 13 cells was defined, totaling $N = 1,092$ sheet images, which is also used for within-group correlation summaries (base data, $N = 13$; Fig. 6). This subset covers the full sampled range of temperatures (−20°C to −5°C) and charging rates (1 C to 4 C) as defined by the experimental condition matrix (Fig. 3). All images from a given cell (including front/back sheet orientation) were kept together when forming this base set to avoid unintended mixing at the cell level.

2.3. Latent feature extraction

In machine learning (ML) and deep learning (DL), supervised methods learn mappings from labeled inputs to outputs, whereas unsupervised methods infer structure directly from unlabeled data. Because labeling subtle plating cues is infeasible and error-prone, unsupervised models are used to uncover the underlying structure. A variational autoencoder (VAE) [32] was selected for its capacity to compress high-dimensional images into a lower-dimensional latent space while preserving essential morphological information. The resulting latent space preserves essential morphology while suppressing noise and redundancy, facilitating downstream tasks such as clustering, anomaly detection, and visualization of plating-related variability. By probabilistically modeling the data distribution, VAEs efficiently capture the variability induced by factors such as charging cycles, temperature, and usage patterns, all of which are crucial in understanding lithium plating and overall battery health [32,42,43]. In contrast to convolutional neural networks (CNNs) that require labeled data [44] or generative adversarial networks (GANs) [45] that can be unstable to train [46], VAEs provide a balance between stability, interpretability and generative capability [32]. Their capability to extract and interpret intricate data patterns in image processing and anomaly detection tasks has been previously demonstrated [47], showing parallel benefits for the post-mortem examination shown here. The choice of a two-dimensional latent space was made to simplify visualization and cluster interpretation. The axes provide a compact map that is easy to visualize and relate to the two dominant operating factors (C-rate and temperature). Clustering in the VAE latent space turns continuous embeddings into pseudo-labels and compact summaries of morphology. Each image or cell is characterized by a vector of cluster proportions, enabling direct comparison across samples and conditions. These summaries support general association analyses with operating covariates (e.g. temperature, C-rate) and response-surface mapping to identify regimes enriched for specific morphologies. Utility is verified via prototype reconstructions and standard validity/stability metrics.

The specific architecture utilized, termed ConvAttnVAE (see Table 1), consists of a convolutional U-Net backbone enhanced with 1-head self-attention. Attention layers capture both local details and long-range dependencies, improving the model's ability to recognize global texture variations indicative of lithium plating. The encoder compresses images to two latent variables (mean and variance), while the decoder reconstructs images from these variables. The reparameterization scheme allows gradients to pass through the stochastic sampling step.

The training configuration is summarized in Table 2. Training used the AdamW optimizer with a learning rate of 1×10^{-5}, $(\beta_1, \beta_2) = (0.9, 0.98)$, and a weight decay of 1×10^{-3}. Early stopping on validation loss prevented overfitting. To improve robustness to illumination and minor geometric variability, common data augmentation techniques were used (random brightness/contrast/saturation, Gaussian blur and noise, random flip). The loss function combined the mean squared error (MSE) for reconstruction accuracy, Kullback–Leibler divergence (KL) to regularize the latent distribution, mutual information (MI) to maximize information preservation and total correlation (TC) to promote disentanglement. A batch size of four and an image size of 960×640 were chosen to balance computational efficiency and reconstruction quality.

A joint embedding strategy was used to make the feature extraction robust. Each training sample consisted of an original image and a version with 10 of the 5-by-5 image tiles randomly masked. Both versions passed through the same encoder, and their latent representations were encouraged to match via a similarity loss. Random masking was applied at every step to expose the model to diverse occlusion patterns, leading to a latent space that generalized well to varying surface textures. The entire training procedure was implemented on an NVIDIA A100 GPU.

Fig. 4 illustrates the operational framework of the ConvAttnVAE model, encompassing both the training and feature extraction phases.

Table 1
ConvAttnVAE architecture summarizing the main components and their functions.

Component	Channels/Dim.	Structure & Parameters	Purpose	Output/Notes
Backbone	–	Conv. U-Net [48] with a self-attention bottleneck [49]; Conv2D uses $k = 3\times3$, $s = (1, 1)$, $p = (1, 1)$	Fuse local + global context	Hierarchical feature maps
Encoder	$16 \rightarrow 512$	6 resolution stages with one ConvBlock per stage and downsampling; GroupNorm (8 groups); attention after last stage; input: 3 channels (RGB), 960×640	Multi-scale feature extraction	$\mathbf{z}_{\mu}$, $\mathbf{z}_{\sigma^2}$
Latent	$d_z = 2$	Reparameterization of $\mathcal{N}(\mathbf{z}_{\mu}, \mathbf{z}_{\sigma^2})$; MLP hidden dim. 256	Compact representation	Latent vector $\mathbf{z}$
Decoder	$512 \rightarrow 16 \rightarrow 3$	Attention at bottleneck followed by 6 resolution stages with upsampling; final Conv2D $k = 3\times3$, $s = (1, 1)$, $p = (1, 1)$	Reconstruction synthesis	$\hat{X}$
Attention	1 head	Multi-head self-attention block with $h = 1$ used symmetrically in encoder/decoder bottleneck	Long-range dependencies	Improves global consistency

Table 2
Optimizer and training configuration for ConvAttnVAE.

Aspect	Settings	Purpose	Effect/Notes
Optimizer	AdamW [50]	Decouple weight decay from gradient update; robust on large nets	Stable, fast convergence on ConvAttnVAE's parameter space
Hyper-parameters	Learning rate $= 1\times10^{-5}$; $(\beta_1, \beta_2) = (0.9, 0.98)$; weight decay $= 1\times10^{-3}$; $\epsilon = 1\times10^{-9}$	Balance speed vs. over-fit; penalize large weights	Promotes smooth training and limits over-saturation of weights
Stability control	*Early stopping* on validation loss	Halt when generalization stops improving	Prevents over-fitting; keeps best checkpoint
Loss function	$\mathcal{L} = \mathrm{MSE} + \mathrm{KL} + \mathrm{MI} + \mathrm{TC}$	Reconstruction accuracy (MSE); latent regularization (KL); informativeness (MI); disentanglement (TC)	Encourages precise reconstructions, smooth latent manifold, independent factors of variation

In Fig. 4a, the training phase is illustrated. The encoder processes an input image to produce the mean ($\mathbf{Z}_{\text{mean}}$) and variance ($\mathbf{Z}_{\text{var}}$) vectors, defining the latent Gaussian distribution. A latent vector $\mathbf{Z}$ is then sampled from this distribution. The decoder reconstructs the image from $\mathbf{Z}$, aiming to produce an output that closely matches the original input. Simultaneously, a masked version of the input image is processed in parallel, promoting robustness in feature extraction even when parts of the image are obscured. A joint embedding with random tile masking encourages invariance to occlusions and local surface contaminants by aligning masked/unmasked views in latent space. This dual-input strategy ensures that the encoder learns to capture essential features that are consistent across variations in the input data. In Fig. 4b, the feature extraction phase is displayed. The encoder maps input images into the latent space, with the resulting mean and variance components visualized. The scatter plot shows the distribution of the latent representations, with the mean values plotted in red and the variances in blue. This visualization provides insights into how the model interprets the data, with clusters indicating groups of images with similar features and the spread of variances reflecting the model's confidence in its representations.

2.4. Clustering in latent space

To interpret the learned latent representation, k-means clustering was performed on the two-dimensional latent coordinates. The number of clusters, $k = 13$, was chosen to correspond to the 13 combinations of temperature and C-rate in the dataset, facilitating direct comparison with experimental conditions. This clustering identified groups of latent points that shared similar morphological characteristics. The presence of a small cluster of outliers underscored the algorithm's ability to detect unusual images (e.g. black outer anode sheets). Exploring alternative cluster numbers is possible and could reveal additional structure. However, $k = 13$ provided a good interpretable partition for the present dataset.

Overall, the methodological choices were guided by two key goals: extracting informative features from high-resolution electrode images and enabling reproducible, interpretable analyses of lithium plating patterns. The use of a controlled mechanical fixture and climate chamber ensured that electrochemical tests were performed under consistent conditions. High-resolution scanning under an argon atmosphere preserved surface morphology without artifacts. A ConvAttnVAE provided an unsupervised, robust latent representation that could capture subtle morphological variations across thousands of images. Finally, k-means clustering in this latent space made it possible to link morphological trends to specific combinations of temperature and charging rate, thereby connecting imaging observations to experimental variables.

3. Results and discussion

After training the ConvAttnVAE on the full set of high-resolution anode scans, the encoded latent representations and resulting clusters were analyzed to uncover patterns in surface morphology and their dependence on cycling conditions. This section presents the findings and interprets them in context. The subsections below describe the latent embedding and morphological continuum, additional cues captured in the latent space, the dependence of the latent coordinates on operating conditions, the relationship between latent dimensions and electrochemical indicators relative to prior work, and the limitations and future directions suggested by this study.

3.1. Latent embedding and morphological continuum

Encoding high-dimensional anode images into a two-dimensional latent space via the ConvAttnVAE produced a map in which samples cluster according to surface morphology. Applying k-means clustering with $k = 13$ organized the latent points into groups that correspond to distinct morphological states. Fig. 5a displays the latent map colored by cluster labels, while Fig. 5b provides representative images for each

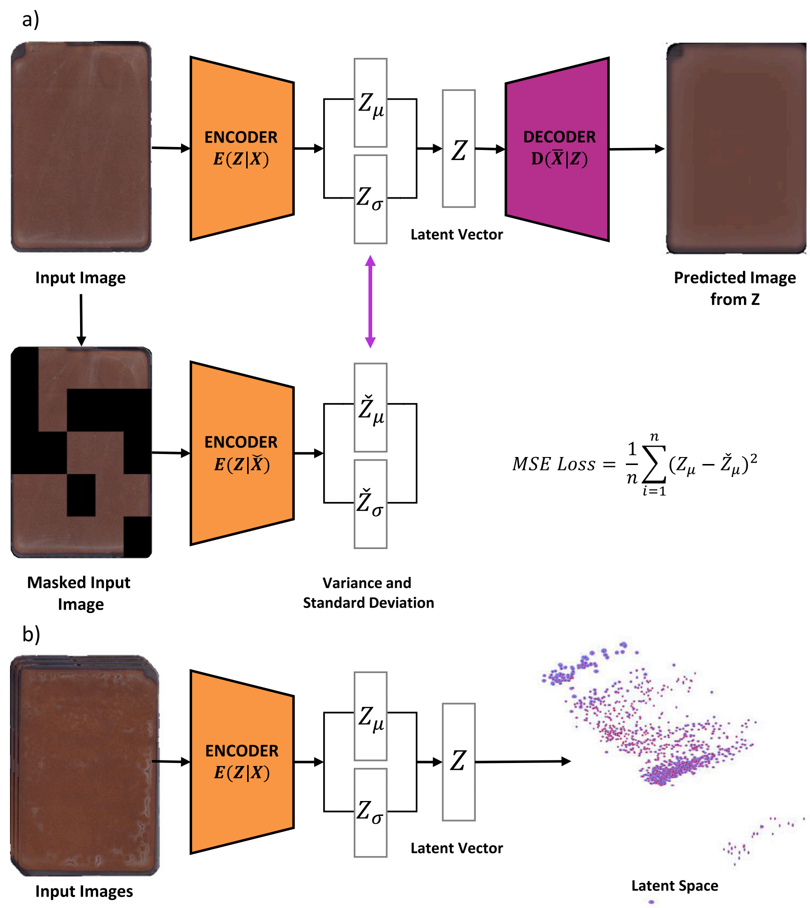

Fig. 4. Operational framework of the ConvAttnVAE model for decoding lithium plating patterns. **(a) Dual-Input Training Strategy:** The training phase employs a self-supervised reconstruction task using both original (X) and masked ($\breve{X}$) electrode images. The network uses an Encoder (E) that maps inputs to a probabilistic latent distribution (defined by mean Z_μ and standard deviation Z_σ). To ensure robust feature learning, a Mean Squared Error (MSE) loss is applied specifically to minimize the discrepancy between the latent means of the full (Z_μ) and masked ($\breve{Z}_\mu$) inputs, forcing the model to infer missing morphological context. **(b) Feature Extraction Phase:** Post-training, the fixed Encoder projects new input images into the low-dimensional latent space (Z). This projection clusters electrodes based on morphological similarity, establishing a "plating space" (visualized here with mean and variance components) for subsequent severity analysis and classification.

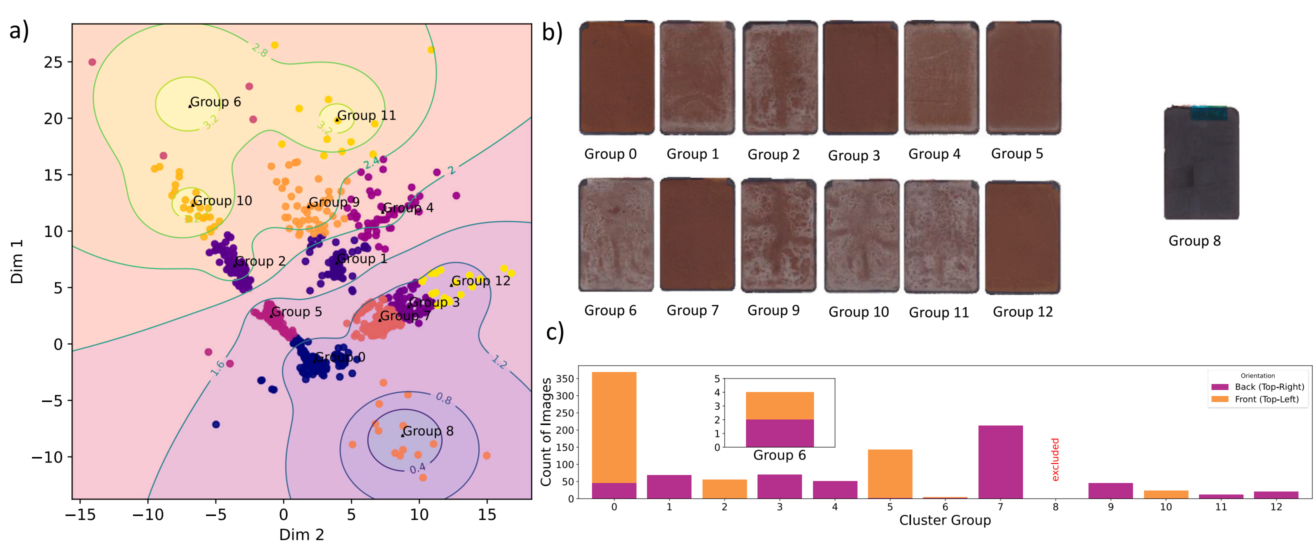

Fig. 5. Latent representation of anode images. **(a)** Two-dimensional latent space of VAE-encoded anode images colored by k-means clusters (k = 13, each group one color). Shading denotes group-wise mean plating severity k^* (0–5; 0 = excluded group). **(b) Representative samples from each cluster (0–12).** Groups span clean surfaces to heavy, granular plating; Group 8 shows dark outer anodes (out of domain). **(c) Quantitative orientation features.** Stacked bar chart of front (top-left overhang) vs. back (top-right overhang) sheets per cluster (N = 1092), verifying that the VAE successfully disentangles geometric orientation. (For interpretation of the references to color in this figure legend, the reader is referred to the web version of this article.)

Table 3
Cluster-wise morphology and plating severity. The mean plating severity k^* increases from clean surfaces (Groups 0, 3, 7, 12) to severe granular deposits (Groups 9–11), with Group 6 capturing rare extreme cases. Group 8 contains dark out-of-domain images. The ordered progression of groups and the monotonic rise in mean k^* indicate that the clusters act as discrete samples along an underlying continuum of plating severity and texture heterogeneity, rather than as hard physical classes.

Group	Images	Visual traits	Plating severity [0–5]	Morphology descriptor
0	369	Uniform reddish–brown surface	0.96	Slight lithium plating at the borders
1	69	White deposits from the borders	1.72	Visible lithium plating at the borders; plating in the center
2	56	White deposits with organic structures	2.55	Strong lithium plating
3	70	Uniform reddish–brown surface	1.01	Slight lithium plating at the borders
4	51	White deposits from the borders	2.05	Visible lithium plating at the borders; plating in the center
5	143	Uniform reddish–brown surface	1.43	Early lithium plating at the borders
6	4	Strong white deposits with organic structures	3.39	Extreme lithium plating
7	213	Uniform reddish–brown surface	1.00	Slight lithium plating at the borders
8	14	Dark images	N/A	Out-of-domain images; black outer anode sheets
9	46	White deposits with organic structures	2.79	Strong lithium plating
10	24	Strong white deposits with organic structures	3.36	Extreme lithium plating
11	12	Strong white deposits with organic structures	3.31	Extreme lithium plating
12	21	Uniform reddish–brown surface	1.02	Slight lithium plating at the borders

cluster. Clusters containing clean, reddish–brown surfaces with minimal plating occupy one region of the latent space (Groups 0, 3, 7, 12), whereas clusters with strong, white, granular deposits occupy another (Groups 9–11). Transitional states (Groups 5, 1, 4) lie between these extremes, and a small cluster of extreme cases (Group 6) shows the highest plating severity. Group 8 highlights the outer anode sheets with dark and uneven textural features. The diversity in surface conditions reflects unique clustering in the latent space. Finally, Fig. 5c provides a quantitative analysis of electrode orientation, confirming that the model encodes geometric features (overhang direction) as a discriminative factor, evidenced by the clear separation of front and back samples in e.g., Groups 5 and 7. Importantly, the ordered arrangement of groups from clean to heavily plated, together with the increase in mean k^* across groups (Table 3), supports interpreting the clustered map as a discrete tiling of a continuous morphology–severity manifold rather than a set of mutually exclusive classes. Here, k^* denotes an externally defined plating-severity grade used only for post-hoc interpretation. In contrast, the unsupervised clusters act as pseudo-labels that discretize the continuous manifold and may therefore split a coarse visual “morphology” into multiple subgroups (e.g., due to differences in texture, spatial distribution, or imaging/orientation cues). Additionally, Fig. 5a underlays an elevation map of the mean k^*-value per group (introduced in [15]: $k^* = 0$ excluded; $k^* = 1$ lithiated graphite/no plating; $k^* = 2$–4 increasing plating; $k^* = 5$ strongest), which visualizes how plating severity varies smoothly along this latent continuum.

These observations are quantified in Table 3, which lists the number of images, visual traits, mean plating severity k^*, and morphology descriptors for each cluster. The mean plating severity increases monotonically from Groups 0, 3, 7, and 12 ($k^* \approx 1.0$) through Groups 5, 1, and 4 to Groups 9–11, with Group 6 exhibiting the highest severity. The arrangement of clusters along a smooth trajectory in latent space thus reflects a continuum from clean to heavily plated surfaces.

This latent continuum links morphology directly to plating severity, offering a compact description of degradation. Rather than handcrafting features or labeling images, the unsupervised approach discovers a progression consistent with electrochemical expectations: mild conditions yield uniform surfaces, while harsh conditions produce granular deposits. Such an interpretable latent coordinate could inform diagnostics by ranking surfaces according to plating severity.

3.2. Additional cues and out-of-domain images

Beyond plating, the latent space captures systematic imaging cues. Groups 5 and 7 share a distinct “black overhang” orientation. The overhang appears in the upper left corner of Group 5 samples and in the upper right corner of Group 7 samples. This symmetry indicates that the VAE learned orientation-dependent features without supervision, separating images not only by plating severity but also by imaging orientation. Group 8 consists of a few dark, out-of-domain images that differ qualitatively from all others. Their separation underscores the model’s ability to isolate atypical samples and suggests caution in interpreting such outliers.

These additional cues highlight the richness of the latent representation. The model captures variations in orientation and imaging artifacts along with morphological differences, implying that careful preprocessing and calibration are critical when extending the approach to other datasets or imaging setups.

3.3. Dependence on operating conditions

Aggregating latent coordinates by cycling temperature and C-rate reveals systematic relationships between operating conditions and latent dimensions. Fig. 6e summarizes the latent coordinates across all tested conditions. Points corresponding to identical temperature and C-rate cluster closely, indicating low within-condition variability. A dominant temperature gradient is visible: colder conditions shift samples toward higher Dimension 1 and lower Dimension 2. Superimposed on this, increasing C-rate primarily increases Dimension 1 (with a smaller, temperature-dependent effect on Dimension 2).

This behavior is quantified in Fig. 6a–d. At fixed temperatures, Dimension 1 increases with C-rate (a: $\rho = 0.1395$, p = 0.65), with steeper slopes at colder temperatures, whereas Dimension 2 shows weak and temperature-dependent/non-monotonic dependence on C-rate (b: $\rho = 0.1110$, p = 0.72). At fixed C-rates, Dimension 1 decreases with increasing temperature (c: $\rho = -0.7885$, p = 0.0014), while Dimension 2 increases with increasing temperature (d: $\rho = 0.7060$, p = 0.0070), with pronounced non-linearities at low rates. Here ρ is Spearman’s rank correlation: +1 denotes a perfect increasing monotonic association, −1 a perfect decreasing monotonic association, and p is the two-sided p-value for testing $\rho = 0$. To robustly quantify these relationships, three complementary correlation coefficients are reported. Pearson’s r measures linear association and is sensitive to outliers but provides an interpretable effect size when trends are approximately linear. Spearman’s ρ_s is rank-based and captures monotonic relationships (including nonlinear but monotonic trends) with reduced sensitivity to scaling and outliers. Kendall’s τ is also rank-based and measures the consistency of pairwise ordering, often remaining stable for small sample sizes and in the presence of ties. Because the latent–condition dependencies can be nonlinear, temperature-dependent, and occasionally influenced by leverage points, relying on a single metric can be misleading. Therefore, the mean absolute values of r, ρ_s, and τ are averaged into a combined score, providing a direction-agnostic and more robust summary of association strength across subgroups. The combined within-group correlation scores in Fig. 6f confirm that temperature is the dominant factor (Combined: 0.93 for Dim1 vs. Temp; 0.84 for Dim2 vs. Temp), while C-rate effects are weaker globally but

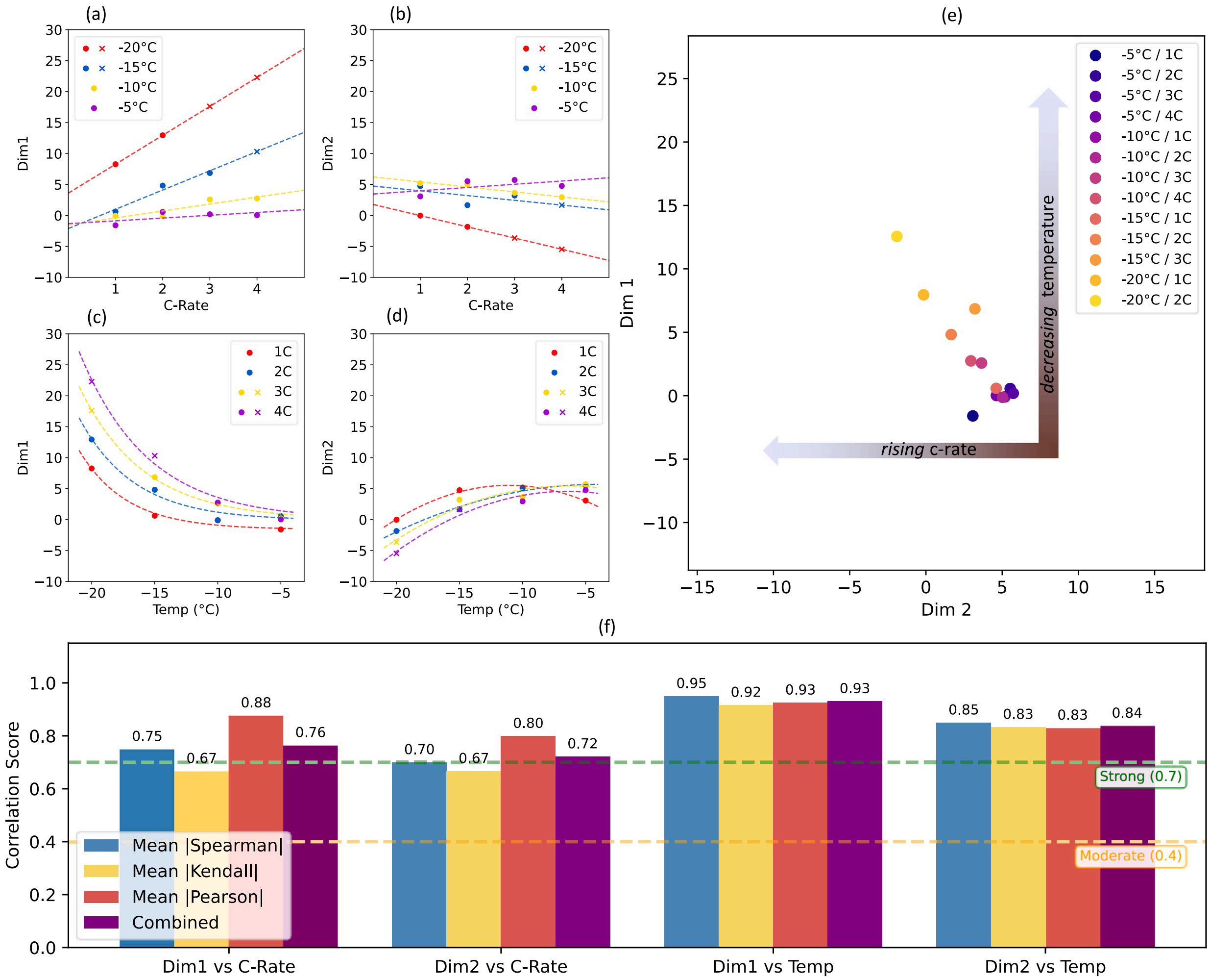

Fig. 6. **(a–b)** C-rate dependence of latent dimensions at fixed temperatures. Dim 1 increases monotonically with C-rate, particularly at low temperatures; Dim 2 displays non-monotonic behavior with temperature-dependent slopes. **(c–d)** Temperature dependence of latent dimensions across C-rates. Dim 1 decreases exponentially with temperature, whereas Dim 2 generally increases as temperature decreases, with pronounced non-linearities at low rates. **(e)** Latent space overview. Points represent means of each cell's latent coordinates, labeled by temperature and C-rate. Identical axis limits facilitate comparison. **(f)** Within-group correlation summary (base data, $N = 13$). Bars report the mean absolute correlation across homogeneous subgroups: for DimX vs. C-rate, correlations are computed within each temperature group and then averaged; for DimX vs. temperature, correlations are computed within each C-rate group and then averaged. Shown are $\overline{|\rho_s|}$ (Spearman), $\overline{|\tau|}$ (Kendall), and $\overline{|r|}$ (Pearson). The purple bar is the combined score $\left(\overline{|\rho_s|} + \overline{|\tau|} + \overline{|r|}\right)/3$. Numbers above bars denote the corresponding values; dashed lines indicate the "moderate" and "strong" interpretation thresholds.

become strong after stratification by temperature (Combined: 0.76 for Dim1 vs. C-rate; 0.72 for Dim2 vs. C-rate). Missing data at the most extreme combinations (3–4 C at −15 and −20°C) were interpolated and are marked with "x".

By mapping operating conditions to latent coordinates, the approach enables a direct visualization of stress factors in the latent space. Clusters corresponding to mild conditions occupy one region, while clusters for harsh conditions occupy another, suggesting that the latent representation could be used to generate risk maps over the temperature–C-rate plane or to screen fast-charging protocols before deployment.

3.4. Relationship to electrochemical indicators

To further interpret the latent dimensions, they were compared with independent electrochemical measures of plating severity. Fig. 7 plots Dimensions 1 and 2 against the stripping capacity Q_{strip} for various temperatures and C-rates (data for 1 C and −20°C were unavailable). Dimension 1 generally increases with Q_{strip} across conditions (top row), while Dimension 2 tends to decrease (bottom row), although the slopes vary with temperature and rate. These monotonic relationships suggest that Dimension 1 is sensitive to plating severity and coverage, whereas Dimension 2 reflects stress-induced loss of uniformity. The interpretation follows from the role of Q_{strip} as an electrochemical proxy for the amount of metallic Li removed from the graphite anode (negative electrode) during the recovery step (approximately proportional to plated volume, i.e. coverage × thickness). The near-monotonic increase of Dim 1 with Q_{strip} across operating conditions therefore indicates that this coordinate encodes the extent of plating visible in the images, such as the areal fraction and coalescence of bright plated regions, so larger Dim 1 values correspond to greater plating severity and coverage.

By contrast, the systematic decrease of Dim 2 with Q_{strip} points to sensitivity not to quantity but to spatial organization. As plating intensifies (especially at low temperature and high C-rate), local current-density gradients and mechanical constraints promote heterogeneous deposition, fracture, and granular textures, i.e. a stress-induced loss of surface uniformity. The encoder maps this deterioration of uniformity onto Dim 2, yielding lower Dim 2 values for larger Q_{strip}. This reading is consistent with the progression from smooth to granular morphologies across clusters in Fig. 5 and with the temperature- and rate-dependent trends in Fig. 6.

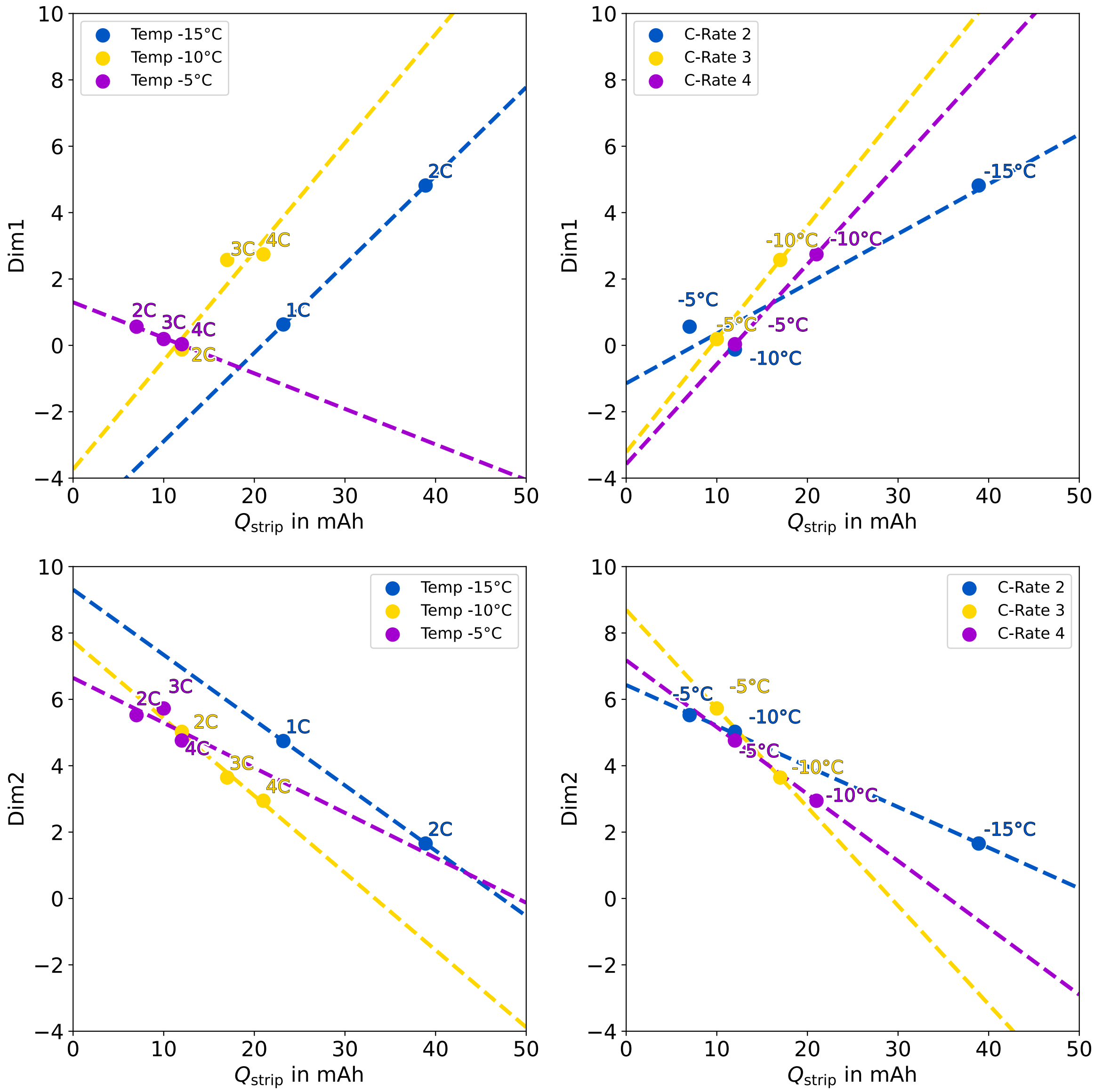

Fig. 7. Relationship between VAE-derived latent dimensions and Q_{strip} under varying temperatures and charging C-rates. Data for 1 C and −20°C are excluded due to lack of Q_{strip} measurements. **Top left:** Dimension 1 vs. Q_{strip} at different temperatures. **Top right:** Dimension 1 vs. Q_{strip} at different charging C-rates. **Bottom left:** Dimension 2 vs. Q_{strip} at different temperatures. **Bottom right:** Dimension 2 vs. Q_{strip} at different charging C-rates.

These findings align with prior work. Ditler et al. [15] reported that colder temperatures and higher C-rates increase Q_{strip}, extend stripping time t_{strip}, and amplify irreversible plating. The latent dimensions reproduce these trends using image data alone, demonstrating that unsupervised deep learning can capture electrochemical behavior from morphological cues. A single exception is the −5°C series (top-left panel of Fig. 7), where the fitted Dim 1–Q_{strip} relation shows a slight negative slope. This deviation is small compared to the consistent monotonic trends observed across the remaining temperatures and C-rates. In the latent map and temperature/C-rate summaries, the −5°C samples occupy a comparatively compact region with a compressed dynamic range (Figs. 5 and 6), so the fitted slope in this panel is more sensitive to residual variation within the sample cloud. Accordingly, the −5°C case is interpreted as exhibiting limited latent contrast for distinguishing operating-condition differences, rather than as evidence for a reversal of the overall plating-severity trend with Q_{strip}.

By relating latent coordinates to physical indicators, the study establishes its contribution within the broader literature on lithium plating diagnostics. Previous approaches have relied on electrochemical signatures, microscopy, or supervised models. Here, an unsupervised method extracts meaningful descriptors that agree with known plating trends and provide additional insight into morphology. While Q_{strip} is a useful cell-averaged proxy for reversible plated Li, it neither localizes plating nor quantifies spatial heterogeneity; in contrast, the proposed imaging latent space provides complementary morphology-based coordinates for severity and uniformity and enables scalable risk mapping and protocol screening from post-mortem scans, including cases where Q_{strip} is unavailable or not fully specific.

3.5. Limitations and future directions

These findings were obtained within a deliberately scoped operating matrix. To respect voltage limits, the coldest and highest-rate corners were not cycled (Fig. 3). As a result, extrapolation beyond the sampled domain is not supported. The two-dimensional VAE embedding was selected for interpretability. Because Q_{strip} aggregates multiple contributions, reversible and irreversible processes may co-vary, so assignments of Dimensions 1–2 to specific mechanisms should be treated as provisional. The present analyses emphasize post-mortem surfaces, which complement but do not fully represent in situ or subsurface behavior. Practical factors (initial state of charge, rest periods, and cell-to-cell variation) were held within typical ranges rather than fully orthogonalized.

Lithium plating is fundamentally an anode-side phenomenon (graphite interface), independent of the cathode chemistry. Plating manifests on the anode across common cell chemistries (e.g., LCO, NMC, LFP). Accordingly, the framework (unsupervised image feature extraction and latent-space analysis) is expected to transfer to other chemistries and form factors (pouch, cylindrical, prismatic). However, the trained mapping is dataset- and morphology-dependent. Retraining or lightweight adaptation (e.g., fine-tuning the encoder) will likely be required to accommodate chemistry- and format-specific texture statistics and imaging setups.

The present modality (post-mortem flatbed optical scans) captures surface texture but cannot, by itself, resolve whether a plated morphology corresponds to reversible or irreversible Li deposition or to mechanical fracture features. In other words, "plating is plating" at the level of these images; discrimination of reversibility arises during (re-)cycling and quantification of stripping behavior. Accordingly, mechanism-specific labels are required. Future work will pair latent features with electrochemical time-series (e.g., decomposing Q_{strip} into reversible/irreversible contributions or using t_{strip}) and, where available, targeted annotations or complementary modalities to enable supervised or weakly supervised separation of these categories.

These characteristics define clear opportunities for extension. Future work can expand the operating space, including cold and high-C-rate regimes, evaluate additional chemistries, and pair latent features with more specific labels, such as irreversible plating capacity or stripping time, to better disentangle overlapping mechanisms. Alternative representation-learning strategies, including supervised, contrastive, or physics-informed objectives, may refine the mapping from morphology to electrochemical behavior. Integrating electrochemical time-series data, impedance spectra, and other sensing modalities into a multimodal encoder could enrich the latent space and improve interpretability. Evolving the descriptive latent map into a calibrated predictive tool may enable risk maps and accelerated screening of fast-charging protocols for safer, more efficient operation. Because the present study is based on offline, destructive post-mortem imaging, the latent features are not directly available to an on-board battery management system (BMS). Instead, they can serve as morphology-derived reference targets to train and calibrate BMS-compatible models from non-invasive signals (e.g., voltage/current/temperature/impedance) or to validate operando sensing modalities in future work.

4. Conclusion

This study presents an automated, label-free post-mortem computer vision framework that couples a convolutional attention-based variational autoencoder with *k*-means clustering to decode and quantify lithium-plating morphology in high-resolution electrode scans at scale. Trained on scans from more than 60 cells cycled across temperatures and charge rates with 84 sheets per cell, the framework learns from flatbed imagery without manual labels and recovers expected condition–morphology trends, with stronger plating at lower temperatures and higher C-rates. The learned two-dimensional latent space organizes a continuum from clean to heavily plated surfaces, disentangles operating conditions (temperature and charging C-rate), and tracks plating severity and heterogeneity. The latent coordinates correlate with the operation conditions (Temperature and C-Rate) and also with stripping capacity Q_{strip}, turning qualitative texture into compact, quantitative, and interpretable descriptors of degradation severity and uniformity.

The framework supports image-based battery diagnostics by enabling unsupervised, scalable characterization of plating without manual labels, producing morphology-consistent clusters that separate operating conditions and reliably flag out-of-domain cases, and providing low/dimensional latent coordinates that act as actionable features for protocol screening, risk mapping, and state-of-health assessment. By linking surface morphology to electrochemical behavior in a compact representation, it supports safer and more durable lithium-ion systems through informed fast-charge design and integration into diagnostic and control workflows.

These inferences should be interpreted in light of several constraints: the dataset provides limited coverage of extreme temperature–rate combinations, unsupervised VAEs can exhibit residual entanglement and the aggregate stripping metric is not fully specific, post-mortem imagery emphasizes surface expression relative to in-situ or subsurface processes, the results can be sensitive to architectural and training choices and residual confounders, such as initial state of charge, rest periods, and cell-to-cell variation, may influence the learned representations.

Future work may align latent features with task-specific targets to improve the separation of underlying mechanisms. The operating space and cell chemistries can be broadened to assess generalization, and alternative clustering approaches and model capacities can be compared. In parallel, multimodal encoders that fuse diverse measurements, such as electrochemical time-series and complementary sensing, could be explored. Incorporating supervised, contrastive, or physics-informed objectives may help calibrate the link between latent variables and mechanistic indicators. The resulting framework aims to evolve the current descriptive map into a predictive tool for protocol design, diagnostics, and safety assessment.

The results establish a robust, interpretable, and extensible pathway from post-mortem anode images to quantitative indicators of lithium plating. The proposed framework consistently organizes morphology along axes that reflect electrochemical severity and uniformity, enabling unsupervised screening of operating conditions and rapid identification of risk. By compressing rich texture into actionable latent coordinates, the method converts qualitative evidence into features suited for diagnostics, control, and fast-charge protocol design. Despite acknowledged limitations, the approach is immediately useful in laboratory workflows and provides a strong foundation for multimodal, predictive battery health analytics. In short, this study turns descriptive imaging into a practical tool for safer, more durable lithium-ion systems.

CRediT authorship contribution statement

Thorsten Tegetmeyer-Kleine: Writing – original draft, Visualization, Software, Methodology, Investigation, Data curation, Conceptualization. **Heinrich Ditler:** Writing – review & editing, Writing – original draft, Visualization, Methodology, Data curation. **Gereon Stahl:** Writing – review & editing, Project administration. **Christiane Rahe:** Writing – review & editing, Project administration. **Dirk Uwe Sauer:** Supervision, Funding acquisition. **Weihan Li:** Writing – review & editing, Supervision, Funding acquisition.

Declaration of competing interest

The authors declare that they have no known competing financial interests or personal relationships that could have appeared to influence the work reported in this paper.

Acknowledgments

The authors gratefully acknowledge the financial support by the Federal Ministry of Research, Technology and Space, Germany through the project InOPlaBat (BMFTR 03XP0352A) and HiPoBat, Germany (BMFTR 13XP0611D). Open Access funding enabled and organized by Projekt DEAL. The authors would especially like to thank Roman Morozov for the fruitful scientific discussions.

Data availability

Data will be made available on request.

References

[1] J. Fan, S. Tan, Studies on charging Lithium-Ion cells at low temperatures, J. Electrochem. Soc. 153 (6) (2006) A1081–A1092, http://dx.doi.org/10.1149/1.2190029.

[2] D.C. Robertson, L. Flores, A.R. Dunlop, S.E. Trask, F.L.E. Usseglio-Viretta, A.M. Colclasure, Z. Yang, I. Bloom, Effect of anode porosity and temperature on the performance and Lithium plating during fast-charging of Lithium-Ion cells, Energy Technol. 9 (1) (2021) 2000666, http://dx.doi.org/10.1002/ente.202000666.

[3] F. Ringbeck, C. Rahe, G. Fuchs, D.U. Sauer, Identification of Lithium plating in Lithium-Ion batteries by electrical and optical methods, J. Electrochem. Soc. 167 (9) (2020) 090536, http://dx.doi.org/10.1149/1945-7111/ab8f5a.

[4] G. Zhang, X. Wei, X. Tang, J. Zhu, S. Chen, H. Dai, Internal short circuit mechanisms, experimental approaches and detection methods of Lithium-Ion batteries for electric vehicles: A review, Renew. Sustain. Energy Rev. 141 (2021) 110790, http://dx.doi.org/10.1016/j.rser.2021.110790.

[5] C. Hogrefe, T. Waldmann, M. Hölzle, M. Wohlfahrt-Mehrens, Direct observation of internal short circuits by lithium dendrites in cross-sectional lithium-ion in situ full cells, J. Power Sources 556 (2023) 232391, http://dx.doi.org/10.1016/j.jpowsour.2022.232391.

[6] I.D. Campbell, M. Marzook, M. Marinescu, G.J. Offer, How observable is Lithium plating? Differential voltage analysis to identify and quantify Lithium plating following fast charging of cold Lithium-Ion batteries, J. Electrochem. Soc. 166 (4) (2019) A725–A739, http://dx.doi.org/10.1149/2.0821904jes.

[7] D.E. Brown, E.J. McShane, Z.M. Konz, K.B. Knudsen, B.D. McCloskey, Detecting onset of Lithium plating during fast charging of Li-ion batteries using operando electrochemical impedance spectroscopy, Cell Rep. Phys. Sci. 2 (10) (2021) 100589, http://dx.doi.org/10.1016/j.xcrp.2021.100589.

[8] Y. Pan, D. Ren, X. Han, L. Lu, M. Ouyang, Lithium plating detection based on electrochemical impedance and internal resistance analyses, Batteries 8 (11) (2022) 206, http://dx.doi.org/10.3390/batteries8110206.

[9] X. Chen, L. Li, M. Liu, T. Huang, A. Yu, Detection of Lithium plating in Lithium-Ion batteries by distribution of relaxation times, J. Power Sources 496 (2021) 229867, http://dx.doi.org/10.1016/j.jpowsour.2021.229867.

[10] X.-G. Yang, S. Ge, T. Liu, Y. Leng, C.-Y. Wang, A look into the voltage plateau signal for detection and quantification of Lithium plating in Lithium-Ion cells, J. Power Sources 395 (2018) 251–261, http://dx.doi.org/10.1016/j.jpowsour.2018.05.073.

[11] A. Su, S. Mao, L. Lu, X. Han, M. Ouyang, Implanted potential sensing separator enables smart battery internal state monitor and safety alert, eTransportation 21 (2024) 100339, http://dx.doi.org/10.1016/j.etran.2024.100339.

[12] S. Mao, Y. Wang, Y. Lu, Z. Wang, D. Wang, X. Han, Y. Zheng, X. Feng, J. Hua, M. Ouyang, Toward electrode-level management of lithium-ion batteries enabled by long-life potential sensing, Energy Storage Mater. 75 (2025) 104773, http://dx.doi.org/10.1016/j.ensm.2025.104773.

[13] H. Zhao, L. Xiang, B. Cui, Q. Zhou, J. Du, S. Li, Z. Liu, G. Yin, G. Han, C. Du, Operando mapping of the dynamic evolution of spatially inhomogeneous reactions in commercial batteries, Joule 9 (12) (2025) 102201, http://dx.doi.org/10.1016/j.joule.2025.102201.

[14] H. Lin, Y. Hu, Y. Zhou, W. Hu, J. Lin, H. Luo, Y. Jin, D. Zhao, J. Chen, M. Tao, P. Shan, J. Liang, Y. Wei, Y. Yang, Unveiling the onset, evolution, and kinetic factors associated with lithium plating on graphite electrodes in lithium-ion batteries, Adv. Energy Mater. (2025) 202502728, http://dx.doi.org/10.1002/aenm.202502728.

[15] H. Ditler, T. Tegetmeyer-Kleine, G. Stahl, C. Rahe, D.U. Sauer, Lithium plating in commercial lithium-ion cells: An extensive study combining electrical methods with post-mortem analysis, J. Energy Storage 132 (2025) 117706, http://dx.doi.org/10.1016/j.est.2025.117706, URL https://www.sciencedirect.com/science/article/pii/S2352152X25024193.

[16] C. von Lüders, V. Zinth, S.V. Erhard, P.J. Osswald, M. Hofmann, R. Gilles, A. Jossen, Lithium plating in lithium-ion batteries investigated by voltage relaxation and in situ neutron diffraction, J. Power Sources 342 (2017) 17–23, http://dx.doi.org/10.1016/j.jpowsour.2016.12.032, URL https://www.sciencedirect.com/science/article/pii/S037877531631727X.

[17] L. Afonso de Araujo, V. Sarou-Kanian, D. Sicsic, M. Deschamps, E. Salager, Operando nuclear magnetic resonance spectroscopy: Detection of the onset of metallic lithium deposition on graphite at low temperature and fast charge in a full Li-ion battery, J. Magn. Reson. 354 (2023) 107527, http://dx.doi.org/10.1016/j.jmr.2023.107527.

[18] D. Wasylowski, N. Kisseler, H. Ditler, M. Sonnet, G. Fuchs, F. Ringbeck, D.U. Sauer, Spatially resolving lithium-ion battery aging by open-hardware scanning acoustic imaging, J. Power Sources 521 (2022) 230825, http://dx.doi.org/10.1016/j.jpowsour.2021.230825.

[19] D. Wasylowski, S. Neubauer, M.J. Faber, H. Ditler, M. Sonnet, A. Blömeke, P.A. Dechent, A.M. Gitis, D.U. Sauer, In situ tomography of lithium-ion battery cells enabled by scanning acoustic imaging, J. Power Sources 580 (2023) 233295, http://dx.doi.org/10.1016/j.jpowsour.2023.233295.

[20] D. Wasylowski, H. Ditler, M. Sonnet, T. Falkenstein, L. Leogrande, E. Ronge, A. Blömeke, A. Würsig, F. Ringbeck, D.U. Sauer, et al., Operando visualisation of lithium plating by ultrasound imaging of battery cells, Nat. Commun. 15 (2024) 10237, http://dx.doi.org/10.1038/s41467-024-54319-6.

[21] T. Waldmann, C. Hogrefe, M. Fluegel, M. Feinauer, M. Kasper, M. Wohlfahrt-Mehrens, (Invited) lithium plating as a critical ageing mechanism in lithium-ion batteries – detection by advanced methods and mitigation, in: ECS Meeting Abstracts, 2023, URL https://api.semanticscholar.org/CorpusID:267582269.

[22] A. Tomaszewska, R. Doel, M. Parkes, G.J. Offer, B. Wu, Investigating Li plating distribution caused by a thermal gradient through modelling, differential voltage, and post-mortem analysis, in: ECS Meeting Abstracts, 2022, URL https://api.semanticscholar.org/CorpusID:250571201.

[23] G. Fuchs, L. Willenberg, F. Ringbeck, D.U. Sauer, Post-mortem analysis of inhomogeneous induced pressure on commercial lithium-ion pouch cells and their effects, Sustainability 11 (23) (2019) 6738, http://dx.doi.org/10.3390/su11236738.

[24] W. Huang, Y. Ye, H. Chen, et al., Onboard early detection and mitigation of lithium plating in fast-charging batteries, Nat. Commun. 13 (2022) 7091, http://dx.doi.org/10.1038/s41467-022-33486-4.

[25] G. Xu, M. Wang, Y. Song, Y. Wei, D. Ren, C. Wang, J. Wang, X. He, Y. Yang, Visualized detection of Lithium plating on graphite anodes cycled under low temperature and fast charging, Adv. Funct. Mater. (2024) http://dx.doi.org/10.1002/adfm.202412614, Early View (First published: 31 Oct 2024).

[26] P.P. Garg, A. Sarkar, I.C. Nlebedim, P. Shrotriya, Lithium plating induced degradation during fast charging of batteries subjected to compressive loading, 2023, ArXiv Preprint arXiv:2309.15291.

[27] A.J. Smith, Y. Fang, A. Mikheenkova, H. Ekström, P. Svens, I. Ahmed, M.J. Lacey, G. Lindbergh, I. Furó, R.W. Lindström, Localized lithium plating under mild cycling conditions in high-energy lithium-ion batteries, J. Power Sources 573 (2023) 233118, http://dx.doi.org/10.1016/j.jpowsour.2023.233118.

[28] C. Fu, V. Venturi, Z. Ahmad, A.W. Ells, V. Viswanathan, B.A. Helms, Universal chemomechanical design rules for solid-ion conductors to prevent dendrite formation in lithium metal batteries, Nat. Mater. 19 (7) (2020) 758–766, http://dx.doi.org/10.1038/s41563-020-0655-2.

[29] J. Deng, X. Yang, G. Zhang, Simulation study on internal short circuit of Lithium ion battery caused by lithium dendrite, Mater. Today Commun. 31 (2022) 103570, http://dx.doi.org/10.1016/j.mtcomm.2022.103570.

[30] E.A. Holm, R. Cohn, N. Gao, A.R. Kitahara, T.P. Matson, B. Lei, S.R. Yarasi, Overview: Computer vision and machine learning for microstructural characterization and analysis, Met. Mater. Trans. A 51 (2020) 5985–5999, http://dx.doi.org/10.1007/s11661-020-06008-4, URL https://link.springer.com/article/10.1007/s11661-020-06008-4.

[31] J. Stuckner, B. Harder, T.M. Smith, Microstructure segmentation with deep learning encoders pre-trained on a large microscopy dataset, Npj Comput. Mater. 8 (1) (2022) 200, http://dx.doi.org/10.1038/s41524-022-00878-5, URL https://www.nature.com/articles/s41524-022-00878-5.

[32] D.P. Kingma, M. Welling, Auto-encoding variational Bayes, in: International Conference on Learning Representations, ICLR, 2014, URL https://arxiv.org/abs/1312.6114.

[33] M. Caron, P. Bojanowski, A. Joulin, M. Douze, Deep clustering for unsupervised learning of visual features, in: Computer Vision – ECCV 2018, in: Lecture Notes in Computer Science, Vol. 11218, Springer, 2018, pp. 139–156, http://dx.doi.org/10.1007/978-3-030-01264-9_9, URL https://openaccess.thecvf.com/content_ECCV_2018/papers/Mathilde_Caron_Deep_Clustering_for_ECCV_2018_paper.pdf.

[34] I. Rmouque, M. Devanne, J. Weber, G. Forestier, C. Wemmert, Ensemble clustering for histopathological images segmentation using convolutional autoencoders, in: Proceedings of the 11th International Conference on Pattern Recognition Applications and Methods, ICPRAM, SciTePress, 2022, pp. 933–940, http://dx.doi.org/10.5220/0010835300003124.

[35] S. Müller, C. Sauter, R. Shunmugasundaram, N. Wenzler, V. De Andrade, F. De Carlo, E. Konukoglu, V. Wood, Deep learning-based segmentation of lithium-ion battery microstructures enhanced by artificially generated electrodes, Nat. Commun. 12 (1) (2021) 6205, http://dx.doi.org/10.1038/s41467-021-26480-9.

[36] Y. Huang, S. González-Reyna, D. Ushizima, et al., Detecting lithium plating dynamics in a solid-state battery with operando X-ray computed tomography using machine learning, Npj Comput. Mater. 9 (1) (2023) 140, http://dx.doi.org/10.1038/s41524-023-01039-y, URL https://www.nature.com/articles/s41524-023-01039-y.

[37] International Energy Agency, Global EV outlook 2025: Electric vehicle charging, 2025, https://www.iea.org/reports/global-ev-outlook-2025/electric-vehicle-charging. (Accessed 17 September 2025).

[38] ACEA, Charging ahead: accelerating the roll-out of EU electric vehicle charging infrastructure, 2024, Summarizes AFIR requirements, incl. ≥150 kW every 60 km on TEN-T core from 2025. URL https://alternative-fuels-observatory.ec.europa.eu/sites/default/files/document-files/2024-05/Charging_ahead_Accelerating_the_roll-out_of_EU_electric_vehicle_charging_infrastructure.pdf.

[39] P.M. Attia, E. Moch, P.K. Herring, Challenges and opportunities for high-quality battery production at scale, Nat. Commun. 16 (2025) 611, http://dx.doi.org/10.1038/s41467-025-55861-7, URL https://www.nature.com/articles/s41467-025-55861-7.

[40] Z.M. Konz, B.M. Wirtz, A. Verma, T.-Y. Huang, H.K. Bergstrom, M.J. Crafton, D.E. Brown, E.J. McShane, A.M. Colclasure, B.D. McCloskey, High-throughput Li plating quantification for fast-charging battery design, Nat. Energy 8 (5) (2023) 450–461, http://dx.doi.org/10.1038/s41560-023-01194-y.

[41] D. Martín-Yerga, X. Xu, D. Valavanis, G. West, M. Walker, P.R. Unwin, High-throughput combinatorial analysis of the spatiotemporal dynamics of nanoscale Lithium metal plating, ACS Nano (2024) http://dx.doi.org/10.1021/acsnano.4c05001, Early Access. URL https://pubs.acs.org/doi/10.1021/acsnano.4c05001.

[42] Y. Bengio, A. Courville, P. Vincent, Representation learning: A review and new perspectives, IEEE Trans. Pattern Anal. Mach. Intell. 35 (8) (2013) 1798–1828, http://dx.doi.org/10.1109/TPAMI.2013.50.

[43] G.E. Hinton, R.R. Salakhutdinov, Reducing the dimensionality of data with neural networks, Science 313 (5786) (2006) 504–507, http://dx.doi.org/10.1126/science.1127647.

[44] L. Chen, S. Li, Q. Bai, J. Yang, S. Jiang, Y. Miao, Review of image classification algorithms based on convolutional neural networks, Remote. Sens. 13 (2021) 4712, http://dx.doi.org/10.3390/rs13224712.

[45] I. Goodfellow, J. Pouget-Abadie, M. Mirza, B. Xu, D. Warde-Farley, S. Ozair, A. Courville, Y. Bengio, Generative adversarial nets, in: Advances in Neural Information Processing Systems 27 (NeurIPS 2014), Curran Associates, Inc., 2014, pp. 2672–2680.

[46] H.-G. Ham, T. Jun, D. Kim, Unbalanced GANs: Pre-training the generator of generative adversarial network using variational autoencoder, 2020, ArXiv abs/2002.02112. arXiv:2002.02112.

[47] A. Makhzani, J. Shlens, N. Jaitly, I. Goodfellow, B. Frey, Adversarial autoencoders, 2015, ArXiv abs/1511.05644. arXiv:1511.05644.

[48] O. Ronneberger, P. Fischer, T. Brox, U-net: Convolutional networks for biomedical image segmentation, in: N. Navab, J. Hornegger, W.M. Wells, A.F. Frangi (Eds.), Medical Image Computing and Computer-Assisted Intervention – MICCAI 2015, Springer International Publishing, Cham, 2015, pp. 234–241, http://dx.doi.org/10.1007/978-3-319-24574-4_28.

[49] A. Vaswani, N. Shazeer, N. Parmar, J. Uszkoreit, L. Jones, A.N. Gomez, Ł. Kaiser, I. Polosukhin, Attention is all you need, in: Advances in Neural Information Processing Systems 30 (NeurIPS 2017), Curran Associates, Inc., 2017, pp. 5998–6008, URL https://proceedings.neurips.cc/paper_files/paper/2017/file/3f5ee243547dee91fbd053c1c4a845aa-Paper.pdf.

[50] I. Loshchilov, F. Hutter, Decoupled weight decay regularization, 2019, arXiv:1711.05101. URL https://arxiv.org/abs/1711.05101.